ACS APPLIED MATERIALS & INTERFACES

www.acsami.org

Research Article

Controlled Porosity in Ferroelectric $BaTiO_3$ Photoanodes

Adriana Augurio, Alberto Alvarez-Fernandez, Vishal Panchal, Bede Pittenger, Peter De Wolf, Stefan Guldin, and Joe Briscoe*

Cite This: https://doi.org/10.1021/acsami.1c17419

Read Online

ACCESS | Metrics & More | Article Recommendations | Supporting Information

ABSTRACT: The use of ferroelectric polarization to promote electron−hole separation has emerged as a promising strategy to improve photocatalytic activity. Although ferroelectric thin films with planar geometry have been largely studied, nanostructured and porous ferroelectric thin films have not been commonly used in photo-electrocatalysis. The inclusion of porosity in ferroelectric thin films would enhance the surface area and reactivity, leading to a potential improvement of the photo-electrochemical (PEC) performance. Herein, the preparation of porous barium titanate (pBTO) thin films by a soft template-assisted sol−gel method is reported, and the control of porosity using different organic/inorganic ratios is verified by the combination of scanning electron microscopy and ellipsometry techniques. Using piezoresponse force microscopy, the switching of ferroelectric domains in pBTO thin films is observed, confirming that the ferroelectric polarization is still retained in the porous structures. In addition, the presence of porosity in pBTO thin films leads to a clear improvement of the PEC response. By electrochemical poling, we also demonstrated the tuning of the PEC performance of pBTO thin films *via* ferroelectric polarization. Our work offers a simple and low-cost approach to control the morphology optimization of ferroelectric thin films, which could open up the development of materials with great potential for PEC applications.

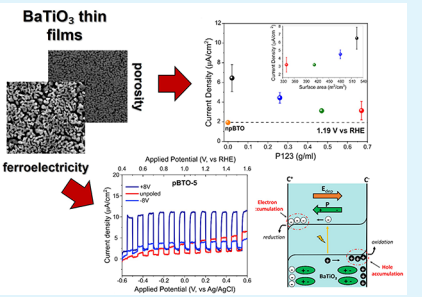

KEYWORDS: *porous ferroelectric thin films, tuning porosity, ferroelectric polarization, piezoresponse force microscopy, electrochemical poling, photo-electrochemical applications*

INTRODUCTION

Photo-electrochemical (PEC) water splitting has recently gained particular attention as a promising approach for the conversion of solar energy into chemical energy.[1,2] To obtain efficient PEC performance, photoelectrodes need to fulfill the following fundamental requirements: chemical stability, good light absorption, and control of the electron−hole recombination rate.[3] Spatial separation of photogenerated charges at the surface of photoelectrodes could reduce the electron−hole recombination losses.[4,5] In this context, one of the approaches that has been regularly adopted to improve photocatalytic activity is the fabrication of porous and nanostructured photoelectrodes. These materials present the advantage of high surface areas, which considerably enhance their reactivity at the electrode/electrolyte interface and their light-harvesting capabilities.[6,7] Moreover, in general, at the nanoscale, a larger number of active sites are present at the surface of these photoelectrodes. This promotes an increase in the surface charge carrier transfer rate, which improves the overall photocatalytic performance.[8]

Recent studies have also focused on the role of ferroelectric polarization in photo-electrocatalysis.[9,10] Ferroelectric materials possess spontaneous polarization which can be reversibly switched by an external electric field.[11] This spontaneous polarization can induce opposite band-bending at the ferroelectric material's surface, facilitating electron−hole pairs' migration toward opposite directions. Thus, the spatially separated photogenerated carriers are able to participate in the oxidation and reduction reactions at different locations.[12] Indeed, it has been demonstrated that the ferroelectric phase of $BaTiO_3$ induces the suppression of charge-carrier recombination, resulting in much higher carrier lifetimes.[13]

Previous research works have reported that redox reactions can occur preferentially on the surface of $BaTiO_3$, $Pb(Zr,Ti)O_3$, and $LiNbO_3$ substrates.[14−17] In particular, Giocondi and Rohrer have shown that when aqueous Ag^+ and Pb^{2+} ions are placed on the BTO surface, upon illumination by ultraviolet light, the oxidation of Pb^{2+} by photogenerated holes and the reduction of Ag^+ by photogenerated electrons generate insoluble products (Ag and PbO_2, respectively), which are selectively accumulated on the surface of the BTO substrate in the proximity of domains with opposite polarization.[12]

This result demonstrates that the polarization from the ferroelectric substrate spatially separates charge carriers,

Received: September 13, 2021
Accepted: January 14, 2022

creating consequently preferred reduction and oxidation sites. More recently, researchers have reported the enhancement of PEC performance in ferroelectric thin films with a planar geometry.[18−20] For example, Cao *et al.* showed that the ferroelectric polarization in $BiFeO_3$ thin films can controllably increase the PEC efficiency, especially after poling pretreatment.[20]

Moreover, Suzuki *et al.* have reported that the addition of porosity in ferroelectric thin films generates an anisotropic strain, which distorts the ferroelectric crystal lattice, promoting the stabilization of the ferroelectric phase.[21] In fact, it has been observed that porous ferroelectric thin films show a higher local piezoelectric response and an enhancement of electromechanical properties compared to dense films.[22−24] On the other hand, it has been demonstrated that ferroelectric spontaneous polarization decreases according to the particle size at the nanoscale. For example, for $BaTiO_3$, it has been reported that the ferroelectric switching disappears in the size range of 5−10 nm.[25] However, to the best of our knowledge, only a small number of studies have been reported on nanostructured ferroelectric thin films for PEC applications.[26−29] For example, Das *et al.* have demonstrated the ability to control the ferroelectric polarization in different morphologies of $BiFeO_3$ nanostructures upon application of an external electric field, which leads to the tuning of the PEC performance depending on the polarization orientation.[28] Moreover, Singh *et al.* have reported that a nanoporous ferroelectric structure of Ag,Nb-codoped $SrTiO_3$ films show an enhancement of the PEC properties, thanks to their large surface areas combined with ferroelectric polarization. Interestingly, the porosity can be controlled by adjusting the sacrificial nanopillar structures, and the annealing parameters and the PEC response can be tuned by applying an electric field, which polarizes the nanocomposite film.[26] Thus, it is of great interest to study the impact of porosity on ferroelectric thin film photoelectrodes, which are very favorable in photoelectrocatalysis.

For these reasons, in the present work, we develop and study porous $BaTiO_3$ (pBTO) thin films as photoanodes, prepared by a soft template-assisted sol−gel method, which allows large-scale coating capability and precise control of the chemical composition.[30,31] We show that it is possible to tune the porosity in $BaTiO_3$ thin films using a facile and low-cost approach while retaining ferroelectric polarization. Importantly, we further demonstrate that the PEC performance can still be controlled *via* the ferroelectric polarization in porous $BaTiO_3$ thin films using electrochemical (EC) poling of the porous films. This paves the way for morphology optimization of ferroelectric photoelectrodes, thus improving their capabilities for PEC applications.

EXPERIMENTAL SECTION

Preparation of pBTO Thin Films. pBTO thin films were prepared by a soft template-assisted sol−gel method.[21,32] All chemicals were purchased from Sigma-Aldrich unless otherwise stated.

1 × 2 cm^2 fluorine-doped tin oxide (FTO) glass (Sigma-Aldrich, SKU 735167-1EA, $L \times W \times$ thickness 300 mm × 300 mm × 2.2 mm, surface resistivity ∼ 7 Ω/sq) substrates were sonicated sequentially in deionized (DI) water, acetone, and 2-propanol for 15 min each. Between each step, FTO glass substrates were blown with nitrogen, in order to remove any possible dust/particulates deposited. In order to prevent charge recombination at the interface between the pBTO layer and the FTO glass,[33] pBTO thin films were grown on compact titanium dioxide (TiO_2) used as a blocking layer (TiO_2/pBTO). The TiO_2 precursor solution was prepared from a titanium isopropoxide (0.2 M) solution in ethanol, with the addition of HCl (0.02 M). After that, the TiO_2 precursor solution was deposited by spin-coating (4000 rpm, 30 s), and was heated at 120 °C for 10 min and then at 500 °C for 30 min.[34]

To prepare pBTO precursor solutions, different quantities of block copolymer (BCP) Pluronic-P123 (0.2, 2, 3.5, 5 g; BASF Corporation) were dissolved in absolute ethanol (3.8 mL) at 40 °C, under stirring (2, 26, 47, 67 w/v %). Then, barium acetate (0.46 g; Thermo Fisher Scientific) was added into glacial acetic acid (3 mL; Thermo Fisher Scientific) at 50 °C under stirring, until complete solubilization. After the solution was cooled down to room temperature (RT), an equimolar amount of titanium butoxide (0.61 g) was added dropwise to the barium acetate solution. The solution was stirred for 30 min at RT. After the Pluronic-P123 solution was cooled down to RT, it was added dropwise under stirring to obtain the final solution. The mixture was stirred for 1 h at RT. Subsequently, the prepared barium titanate precursor solutions were deposited by spin-coating onto the compact TiO_2 layers on FTO glass at 500 rpm, 5 s (1st step) and then 3000 rpm, 30 s (2nd step), successively. The as-prepared thin films were placed on a hot plate at 90 °C for 1 min and then 350 °C for 4 min. After that, the thin films were annealed at 750 °C for 10 min and then cooled at 30 °C, at a ramp rate of 5 °C/min (Lenton Furnace, model UAF 14/5). Hereafter, the TiO_2/pBTO thin films obtained are named pBTO-0.2, pBTO-2, pBTO-3.5, and pBTO-5, according to the quantities of BCP used.

Material Characterization. The morphology of pBTO thin films was investigated by scanning electron microscopy (SEM) on an FEI Inspect F, using an accelerating voltage of 5 kV. The estimation of porosity from SEM images was obtained using ImageJ analysis software, where the pores' area was isolated by thresholding.[35] The analysis was repeated three times for each different pBTO thin film.

The thickness measurements of pBTO thin films were obtained using ImageJ analysis, and they were performed 10 times for each SEM cross-sectional image.

The transmittance of pBTO thin films was measured using a PerkinElmer Lambda 950 UV−vis spectrophotometer in the 300−600 nm range. The optical band gap (E_g) of pBTO thin films was estimated using the Tauc relation,[36] which is expressed as

$$\alpha h\nu = C(h\nu - E_g)^n$$

where C is a constant, α is the absorption coefficient, $h\nu$ is the incident photon energy, and n is related to the type of transition. The direct band gap energy E_g of pBTO thin films was determined by the extrapolated linear region of the plots at $(\alpha h\nu)^2 = 0$.

To determine the overall porosity of pBTO thin films, spectroscopic ellipsometry (SE) measurements using two surrounding mediums (air and water) were carried out using samples deposited on a Si substrate without a compact TiO_2 blocking layer, using a Semilab SE2000 ellipsometer.

For ambient conditions, samples were placed on a hot plate (120 °C, 30 min) before measurements, in order to remove any possible residual water molecules that remained in the pores. Application of the Bruggeman effective medium approximation (EMA) allowed accurate determination of the overall porosity of each pBTO sample.[37] In a subsequent step, and in order to confirm ambient porosity calculations, porous samples were infiltrated with water and SE measurements were fitted again using the same EMA but adding water instead of air as a medium material.[38] The surface area of different porous samples prepared in this work was determined by ellipsometric porosimetry at atmospheric pressure, using water as a solvent.[56] Thus, adsorption isotherm at controllable humidity were fitted using the Brunauer, Emmett, and Teller (BET) model. The cross-section area for water was calculated as 0.105 nm^2 using standard methods.[39] All data analyses were performed using Semilabs SEA software (v1.6.2).

The crystalline phase of pBTO thin films was investigated by X-ray diffraction (XRD) using a PANalytical X'Pert Pro diffractometer,

https://doi.org/10.1021/acsami.1c17419
ACS Appl. Mater. Interfaces XXXX, XXX, XXX−XXX

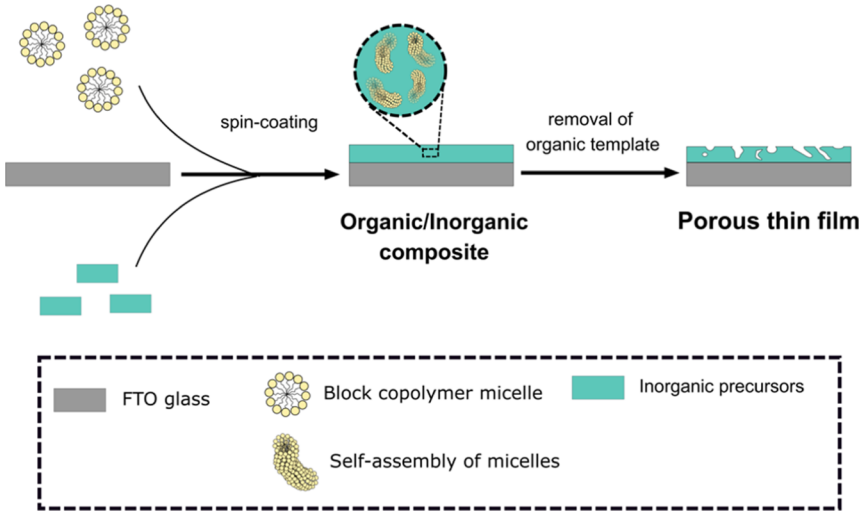

Figure 1. Soft template-assisted sol–gel method used for the preparation of BTO thin films. The procedure involves the following steps: preparation of BTO precursor solution, where the inorganic component and the block copolymer (BCP) agent are combined and the hydrolysis/polycondensation reaction takes place; after that, the BTO precursor solution is deposited on cleaned FTO glass by spin-coating, and the organic/inorganic hybrid film is obtained. Finally, the deposited film is annealed (750 °C, 10 min) to remove the organic template and allow the BTO crystallization, promoting the formation of porous BTO (pBTO) thin films.

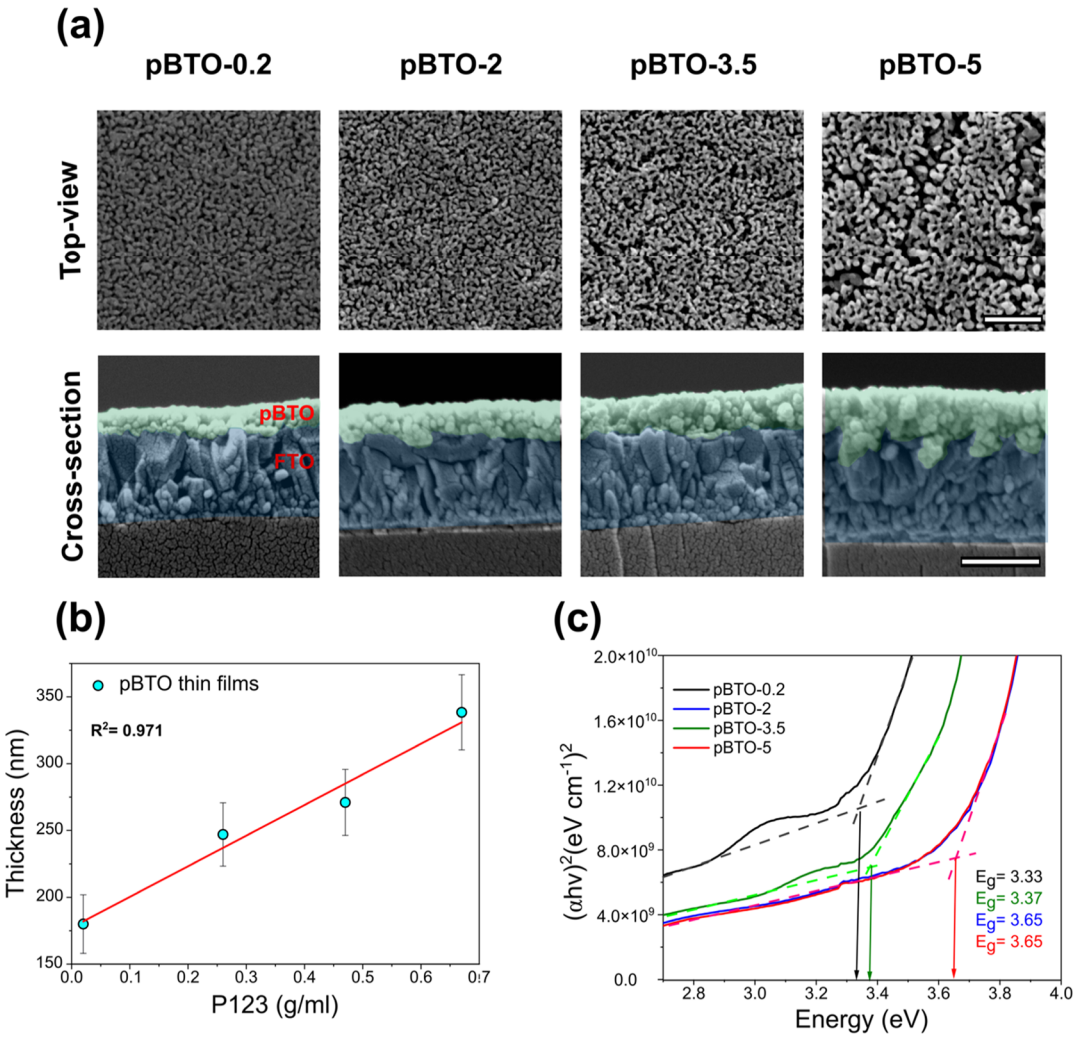

Figure 2. Top-view and cross-sectional SEM images of pBTO thin films, prepared with different amounts of P123 block-copolymer, 0.2–5 g (scale bar: 500 nm) (a); linear relationship between the thickness of pBTO thin films and the concentration (g/mL) of P123 block-copolymer (b); Tauc plot of pBTO thin films, which allows the estimation of their band gap energies (c).

https://doi.org/10.1021/acsami.1c17419
ACS Appl. Mater. Interfaces XXXX, XXX, XXX–XXX

equipped with a Cu Kα source, with a 0.5° grazing incidence angle. The XRD measurements were obtained from 2θ = 20 to 70° with a scan speed of 0.006°/s.

Raman spectroscopy measurements were carried out on a Renishaw inVia confocal Raman microscope, using a 100× objective and 442 nm as the excitation wavelength. The Raman spectra were acquired after setting the accumulation and acquisition time to 3 and 100 s, respectively, in the 100−800 nm range. Piezoresponse force microscopy (PFM) images were recorded using a Bruker Dimension IconXR atomic force microscope to investigate the ferroelectric response of pBTO-0.2 and pBTO-5 thin films. PFM imaging was performed in DataCube mode (DCUBE PFM) by applying a DC voltage sweep to the tip going from −8 to +8 V. DCUBE PFM height, phase, and amplitude signals of pBTO-0.2 and pBTO-5 were acquired off-resonance at 250 kHz and with 4 Vac. The PFM measurement is accurate only when the electrostatic force is zero, that is, when the tip voltage is equal to the surface potential; therefore, hysteresis loops were measured without electrostatic field artefacts by using switching spectroscopy PFM (SS-PFM) mode. This involves applying a series of ("on-field") write voltage segments for each of several ("off-field") read voltages (Figure S1). The purpose of the "on-field" segments is to determine the voltage (between tip and sample) where the polarization state of the material changes. The "off-field" segments allow characterization of the material response after each of the "on-field" segments to look for the state change and measure the material response. By using a series of different "off-field" voltages, it is possible to compensate for electrostatic field artifacts that arise due to the difference in contact potential between tip and sample. During each write and read voltage segments, the amplitude/phase *versus* contact resonance frequency sweeps are performed. These are then fitted and peak amplitude, quality factor, and corresponding phase values are recorded. Plots of amplitude and phase *versus* write voltage are extracted. The SS-PFM data were collected with minimum and maximum *write* voltage segments ranging from −10 and +10 V, respectively, in 50 steps, going from low to high. The write time duration of each segment was 10 ms. The minimum and maximum *read* voltage segments ranged from −4 and +5 V, respectively, in 7 steps, going from low to high. The read time duration of each segment was 20 ms.

PEC measurements were conducted on pBTO thin films with a potentiostat (Gamry Potentiostat Interface 1000) using a three-electrode configuration: a pBTO thin film as the working electrode, Ag/AgCl as the reference electrode, and a platinum wire as the counter electrode. All the PEC tests were performed at RT in 1 M NaOH solution as an electrolyte. A solar simulator (Sciencetech, class: ABA) was used for the front illumination of pBTO thin films. All the PEC measurements were taken at AM 1.5 G 1 sun (100 mV/cm^2).

To acquire linear sweep voltammetry (LSV) curves, the potential was swept from −0.6 to +0.6 V *versus* Ag/AgCl at a rate of 10 mV/s. The LSV measurements were performed in triplicate for each type of the pBTO thin film.

To investigate the effect of ferroelectric polarization on PEC performance, EC poling was carried out on pBTO-0.2 and pBTO-5 using a two-electrode cell configuration. The pBTO thin film and a platinum wire were used as the working electrode and the counter electrode, respectively, in a non-aqueous electrolyte solution (0.1 M $LiClO_4$ in propylene carbonate). The EC poling was conducted using a Keithley 2400 by applying alternatively +8 V/−8 V on a platinum electrode for five steps (10 s each). The last potential was +8 or −8 V to obtain a remnant P_{down} or P_{up}, respectively. The current flow between the sample and the counter electrode was monitored to be not higher than 1 mA in order to avoid damaging the sample.[19,40]

After EC poling, pBTO thin films were washed with DI H_2O, acetone, and ethanol and dried in air before performing LSV measurements.

RESULTS AND DISCUSSION

An overview of the fabrication method is shown in Figure 1. Porous architectures were created following the so-called soft template-assisted sol−gel method. To this end, BCP micelles were mixed in solution with inorganic sol−gel precursors and deposited on FTO substrates. In a subsequent step, the hybrid composites were transformed into the final porous BTO film by thermal calcination. This is in line with previous studies, where controllable porous materials were synthesized using BCPs as sacrificial structure-directing agents. Indeed, following this approach, the pore size can be tuned by controlling the BCP molecular weight[41] or by the addition of swelling agents to the hybrid solution,[42] while the total sample porosity directly relies on the final organic/inorganic ratio.[43]

SEM top-view images confirm the porous structure of pBTO thin films (Figure 2a). In particular, the films show a solid matrix with interconnected pores. Furthermore, it is possible to observe that by increasing the concentration of P123 BCP, the pore area gradually increases (Figure 2a top view). The morphological features are also investigated through cross-sectional SEM images, where the grains are vertically stacked, and the gaps between them are the pores (Figure 2a cross-section). Moreover, the thickness of pBTO thin films is linearly proportional to the P123 BCP concentration, calculated as the quantity of BCP over the total volume of the precursor solution (R^2 = 0.971). This is expected as the volume occupied by the organic sacrificial template present in the thin films deposited by spin-coating is higher in pBTO-5 compared to pBTO-0.2. For this reason, the pBTO-5 thin film is thicker (Figure 2b).

The transmittance spectra of pBTO thin films show band edges within 350−380 nm across the UV light range (Figure S2). It can be observed that the absorption coefficients of the pBTO thin films are higher compared to those reported for ceramic samples[44] but in the same order of magnitude as barium titanate thin films prepared by sol−gel methods.[45−47] Indeed, the preparation technique and the related stoichiometry of the films can influence the optical properties.[48] Moreover, previous research has reported an increment of the absorption coefficient in porous films,[49−51] as the porosity present in the films can act as light scattering centres, resulting in higher absorption of the light.[49] On the other hand, the high absorption coefficient could also be related to the presence of imperfections in the films (*e.g.*, defects, disordering, and oxygen vacancies).[49] The band gap energies estimated from the Tauc plot are in the range 3.3 to 3.6 eV (Figure 2c), which is close to the value reported for bulk samples (3.4 eV),[52] and it is in accordance with values previously reported for BTO thin films prepared by the sol−gel method (3.7 eV).[48] Indeed, it has been found that the preparation technique can induce variations in the stoichiometry and defect distribution of the films, leading to differences in the estimated band gap energies.[48] Moreover, the slight variation between the estimated band gap energy values of pBTO thin films could be related to scattering effects which can arise in porous samples. This has previously been demonstrated to lead to an apparent absorption enhancement due to light scattering, which influences the measured transmittance spectra, including the position of the absorption onset used to determine the band gap[53] (Figure S2).

Ellipsometric assessment of pBTO thin films presented in this work was conducted to verify the control of porosity by

https://doi.org/10.1021/acsami.1c17419
ACS Appl. Mater. Interfaces XXXX, XXX, XXX−XXX

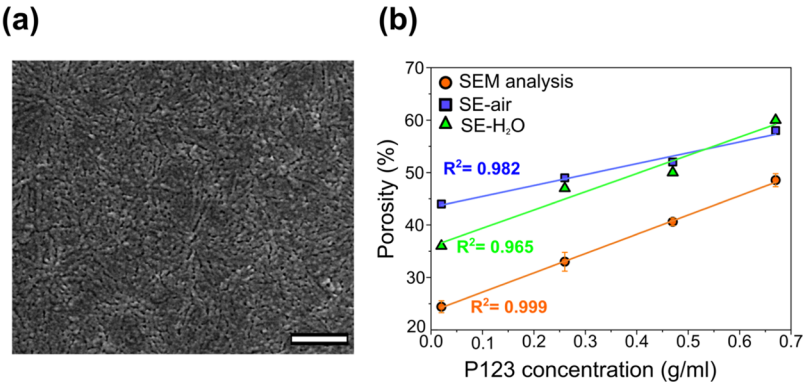

Figure 3. Top-view SEM image of the npBTO sample used as a reference for ellipsometric analysis (scale bar: 500 nm) (a); comparison between porosity (%) values obtained using SEM analysis, SE-air, and SE-H_2O for pBTO thin films with different P123 BCP concentrations (b).

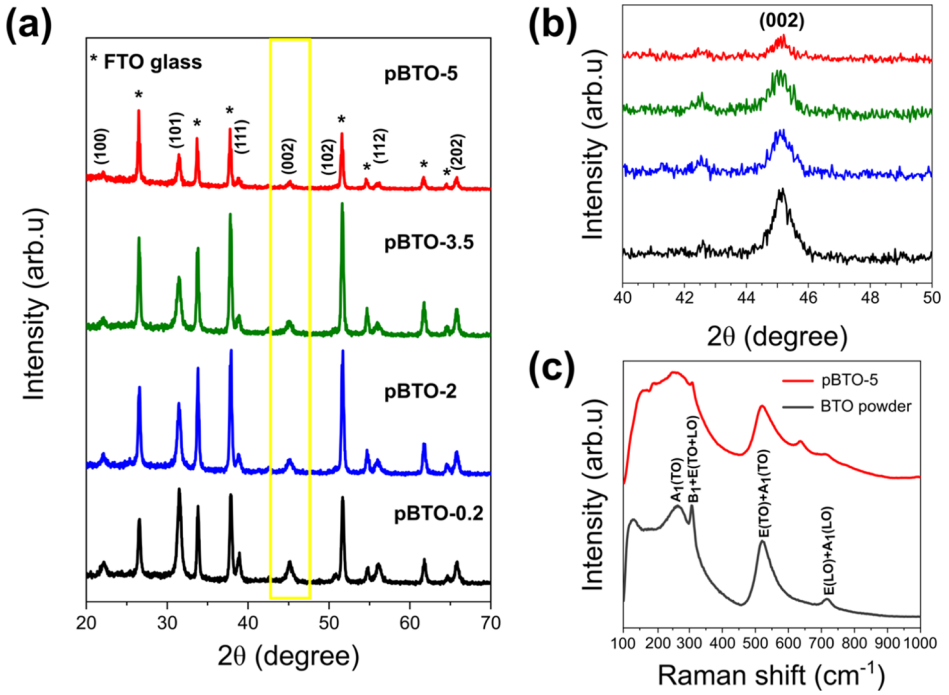

Figure 4. XRD spectra of pBTO thin films (0.2−5) (a) and corresponding enlargement in the 40−50° region (b); Raman spectra of pBTO-5 compared to the reference BTO tetragonal powder (c).

adjusting the P123 BCP concentration. Due to a significant fraction of pores > 50 nm, the determination of pore size distribution via capillary condensation was not applicable, and therefore an alternative approach was followed as shown in Figure S3.[54] In a first step, a non-porous BTO (npBTO) thin film is used to establish the optical characteristics (n and k) of the pristine material (Figure S3(i)). The application of a Cauchy dispersion model displayed a reasonable fit with optical parameters acquired for the npBTO film (Figure S4). The obtained refractive index of the film (1.98 at 632 cm^{-1}) is slightly lower than the one reported in the previous literature (2.33).[55] This small variation can be explained taking into account the presence of certain intrinsic porosity, probably due to the material deposition process by spin-coating, and visible in the corresponding SEM image (Figure 3a). Considering that all BTO samples present in this study are deposited in the same conditions, this residual porosity can be neglected.

The optical parameters of npBTO were used as reference values to determine the porosity in all porous pBTO thin films.

In a second step, pBTO-0.2, pBTO-2, pBTO-3.5, and pBTO-5 samples were characterized following the same SE protocol. In all these cases, ellipsometer angles (Ψ and Δ) were fitted using a Bruggeman EMA to extrapolate the overall porosity of each pBTO sample (Figure S5). Thus, a homogeneous flat layer with a certain volume fraction of each component ($BaTiO_3$ and air) was established (Figure S3(ii)). In the final step, pBTO samples were infiltrated with water to confirm the porosity values previously obtained (Figure S3(iii)). In this case, a homogeneous flat layer with a certain volume fraction of $BaTiO_3$ and water was used as a starting point for the modeling. Similar to the previous case, ellipsometer angles (Ψ and Δ) were fitted using a Bruggeman EMA to determine the overall porosity of each pBTO sample (Figure S6).

Table S1 summarizes the porosity of pBTO thin films obtained using SE-air, SE-H_2O, and SEM analysis. The porosity values acquired by SE-air and SE-H_2O show a linear dependence with P123 BCP concentration, in agreement with

https://doi.org/10.1021/acsami.1c17419
ACS Appl. Mater. Interfaces XXXX, XXX, XXX−XXX

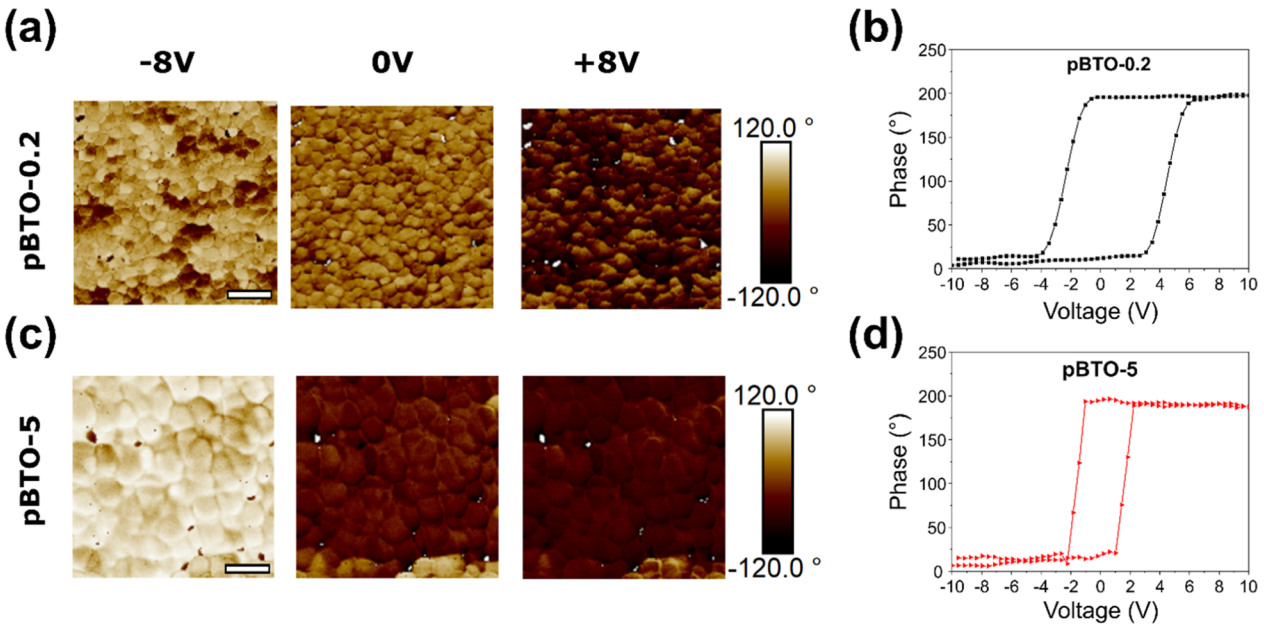

Figure 5. PFM phase signals of pBTO-0.2 and pBTO-5 extrapolated at −8, 0, and +8 V (scale bar: 200 nm), during a ramp from −8 to +8 V (a,c) and the corresponding phase hysteresis loops, measured using SS-PFM (b,d).

the ones estimated from image analysis of the SEM micrographs (Figure 3b). However, in all cases, the porosity values obtained by SE are higher compared to the ones obtained by SEM. We note that the estimation of porosity from SEM images only refers to the surface of the samples, contrary to SE, where the whole film thickness is analyzed,[56] which would account for this systematic underestimation of porosity by SEM analysis.

Porosity values obtained after infiltration (SE-H_2O) show a good reproducibility when compared with the ones obtained for ambient measurements (SE-air), showing in both cases similar values for high and medium P123 BCP concentrations (Figure 3b). However, for low organic content (pBTO-0.2), SE results show a slight discrepancy (36 *vs* 44%). A likely reason for the discrepancy in the pBTO-0.2 sample may be incomplete water infiltration due to limited pore accessibility due to the lower porosity and pore size compared to the rest of the pBTO thin films.

Moreover, the surface area (S) of pBTO thin films was determined from the ellipsometric adsorption isotherms by applying the BET method. Figure S7 shows the BET plots obtained for the samples presented in this work. By fitting the experimental values in the linear range ($0.05 \leq p/p_0 \leq 0.3$), the corresponding surface areas were calculated. A clear reduction in the surface area can be identified with the increase in the concentration of the P123 BCP in the starting solution from pBTO-0.2 (524 m^2/cm^3) to pBTO-5 (340 m^2/cm^3). This is in line with observations by top-view SEM analysis (Figure 2a). Thus, the higher the BCP concentration, the bigger the pores in the final inorganic structure and therefore the lower the surface area.

To investigate the crystalline phase, XRD analysis was performed on pBTO thin films, which clearly show the peaks referred to BTO crystals (Figure 4a). However, it is difficult to discriminate between the cubic (paraelectric) phase and the tetragonal (ferroelectric) phase using XRD. It has been reported that the strain can stabilize the cubic (paraelectric) phase in BTO at RT despite the tetragonal (ferroelectric) phase being the most thermodynamically stable.[57,58] Therefore, it is important to confirm that the pBTO thin films we have produced in this work are tetragonal by analyzing the XRD patters in more detail. In general, compared to the cubic phase, the XRD pattern referred to the BTO tetragonal structure show split peaks at $2\theta = 45°$ into two peaks at $2\theta = 44.8°$ and $2\theta = 45.4°$, which correspond to *hkl* Miller indices (002) and (200), respectively (JCPDS 05-0626). For the pBTO thin films, the presence of this splitting is not distinctly observable, probably because the polycrystalline nature of the film broadened the peak width[59] (Figure 4a). In addition, all of the peaks in the XRD pattern of pBTO-5 show a lower intensity compared to pBTO-0.2, including the peak at $2\theta = 45°$ making the analysis of this peak more challenging (Figure 4b). The overall reduction in XRD signal intensity from $BaTiO_3$ compared to the substrate-related peaks is expected, as when increasing the concentration of P123 BCP the volume fraction occupied by the BTO inorganic precursors present in the film deposited by spin coating is lower, and a higher signal intensity is obtained from the substrate through the pores.

To further investigate the crystalline phase, Raman spectroscopy was performed on the pBTO-5 thin film and commercial BTO powder, annealed at 1200 °C for 12 h, which is used as the reference sample. BTO powder shows the peaks at 275, 305, 520, and 720 cm^{-1}, which are assigned to the $A_1(TO)$, $B_1 + E(TO + LO)$, $E(TO) + A_1(TO)$, and $E(LO) + A_1(LO)$ Raman active modes, which clearly correspond to the tetragonal phase of BTO[60] (Figure 4c).

In the pBTO-5 thin film, the presence of the peaks relative to the Raman modes of tetragonal BTO is confirmed except for the splitting of $A_1(TO)$ mode. This can be attributed to the in-plane compressive strain induced by porosity, which enhances the stability of the ferroelectric phase.[61] We can therefore confirm that the pBTO-5 thin films are in the tetragonal, ferroelectric phase. In addition, the Raman active mode detected at 639 cm^{-1} in the pBTO-5 thin film is most likely attributed to the anatase phase of TiO_2[62] (Figure 4c).

https://doi.org/10.1021/acsami.1c17419
ACS Appl. Mater. Interfaces XXXX, XXX, XXX−XXX

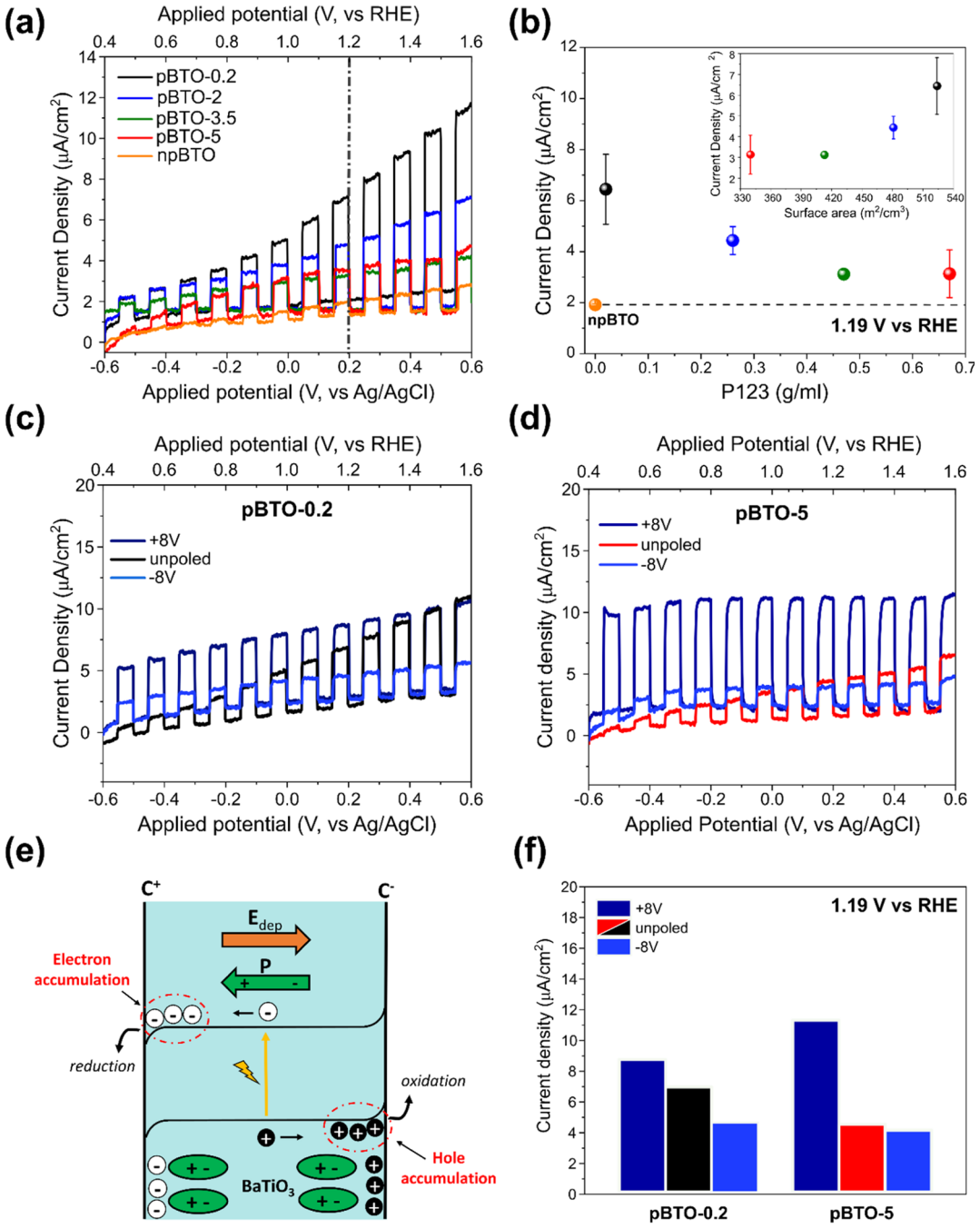

Figure 6. LSV measurements of BTO thin films (a) and relative current density values extrapolated at 1.19 V *vs* RHE (b) and relative correlation with the surface area (inset); LSV curves of pBTO-0.2 (c) and pBTO-5 (d) obtained before and after EC poling and comparison of the current density values obtained at 1.19 V *vs* RHE (f); schematic of the band-bending phenomenon, which occurs at the pBTO/electrolyte interface (e).

To study the ferroelectric response of pBTO thin films, PFM was obtained for pBTO thin films with lower (pBTO-0.2) and higher (pBTO-5) porosity. The topographic images show the grain structure of the pBTO films where the presence of pores is further confirmed. However, the pores are not well-defined, probably because of the use of the PFM contact mode, which is not particularly suitable for the resolution of film topography. Moreover, it is possible to observe that the BTO grain structure is larger in pBTO-5 than in pBTO-0.2, in agreement with SEM images (Figure S8a).

The PFM phase images of pBTO-0.2 and pBTO-5 show clear regions in the samples with different contrast, which reflect grains randomly split into domains of opposite polarities. The dark areas correspond to the domains with polarization oriented toward the substrate (P_{down}). In contrast, the bright regions are domains with polarization terminated at the free surface of the film (P_{up}). As the DC voltage was increased from −8 to +8 V, the domains switched their polarity in both samples (Figure 5a,c). This behavior is also observed in the PFM amplitude images (Figure S8b(i,iii)).

Analyzing the PFM phase images in more detail, the switching of the domains appears more complete for pBTO-5 compared to pBTO-0.2. This evidence could be related to the relationship between grain size and piezoresponse. According

https://doi.org/10.1021/acsami.1c17419
ACS Appl. Mater. Interfaces XXXX, XXX, XXX−XXX

to previous research,[63,64] larger grains usually exhibit stronger piezoresponse signals compared to smaller grains. Therefore, as a consequence, small grains could be more difficult to switch in polarity, with respect to large grains. This result is also reflected in the PEC performance after the EC poling procedure, which is discussed further below.

However, it has been found that surface charging and electrostatic interaction between the tip and the sample can contribute to create contrast in PFM images, which can be unrelated to the presence of ferroelectricity.[65,66] Thus, to confirm the ferroelectric behavior of pBTO thin films, we performed SS-PFM, which removes electrostatic contributions that can affect the signals measured by traditional PFM modes.[67] Figures 5b,d and S8b(ii,iv) show the PFM phase and amplitude hysteresis loops, respectively, acquired using SS-PFM. The phase loops show clear switching with a phase difference of close to 180°, as expected for $BaTiO_3$, and the amplitude loops show a clear "butterfly" shape. These results clearly confirm the ferroelectric properties of the pBTO samples of both high and low porosity. The phase loop is also narrower for pBTO-5 samples, indicating a smaller coercive field, in agreement with the more complete domain switching seen in the PFM images for these samples.

Therefore, we can conclude that the PFM phase and amplitude signals obtained demonstrate spontaneous polarization switching by applying an electric field in pBTO-0.2 and pBTO-5 thin films and the SS-PFM hysteresis loops, in combination with Raman spectroscopy, showing the tetragonal (ferroelectric) phase and EC poling results, that will be discussed further below, give strong evidence in support of the ferroelectricity of these samples.

After confirming the ferroelectric behavior of pBTO thin films, we tested their PEC properties under chopped illumination. All pBTO thin films show higher photocurrent density than the non-porous BTO (npBTO) samples, suggesting that the inclusion of porosity is beneficial. We note that for fair comparison to the pBTO films, the npBTO films used for these tests were deposited on FTO glass with a compact TiO_2 blocking layer. The films still demonstrated a non-porous structure when using these substrates (Figure S9). Moreover, the LSV curve of the compact TiO_2 blocking layer is shown in Figure S10, confirming that no additional contribution in the PEC performance arises from this layer.

Furthermore, from the current density−voltage (J−V) curves of pBTO thin films, it is possible to observe that when increasing the concentration of P123 BCP, the measured current density gradually decreases (Figure 6a), with pBTO-3.5 and pBTO-5 displaying very similar values. When considering the photocurrent values extrapolated at 1.19 V *versus* RHE and obtained across a range of samples, this trend can be seen more clearly (Figure 6b), and it can be seen that the pBTO-3.5 and pBTO-5 indeed show comparable values of photocurrent density within the spread of error across the measured samples. Nevertheless, it is clear that at 1.19 V *versus* RHE, pBTO-0.2 shows an enhancement of the photocurrent of about 3 $\mu A/cm^2$ compared to pBTO-5 (Figure 6b).

This result could be related to the presence of a high number of smaller pores in pBTO-0.2, according to the SEM analysis, which leads to higher surface area and consequently improvement of PEC performance. In contrast, although pBTO-5 shows greater overall porosity, this is comprised of larger pores, which results in a lower surface area overall and a decrement of overall PEC response. This is confirmed by the measured surface area values of pBTO thin films discussed above and reported in Figure S7. From the inset in Figure 6b, it can be seen that the photocurrent density at 1.19 V *versus* RHE shows a good correlation with the surface area of the samples.

Therefore, we can conclude that the introduction of porosity into a BTO photoanode does indeed improve the PEC photocurrent but that a basic increase in overall porosity *via* inclusion of increasing quantities of BCP does not necessarily increase PEC photocurrent further. Instead, careful consideration must be given to the morphology of the porous photoelectrode, where a greater number of smaller pores is preferable, as it leads to an overall increase of interfacial area in contact with the electrolyte.

As previously reported, one of the beneficial and fascinating properties of ferroelectrics as photocatalysts is the ability to switch their photocurrent response *via* controlling the polarization orientation.[68] Therefore, to investigate the effect of ferroelectric polarization on PEC response, we performed EC poling on pBTO thin films at lower (pBTO-0.2) and higher (pBTO-5) porosity and measured J−V curves after the poling pretreatment. Compared to the unpoled state, the +8 V EC poling induces an improvement of PEC performance in both pBTO-0.2 and pBTO-5 (Figure 6c,d). This enhancement in the PEC response can be related to the band-bending at the pBTO/electrolyte interface resulting from the electrical polarization. When pBTO is exposed to illumination, electron−hole (e^-−h^+) pairs are generated and e^- will migrate to the C^+ surface while h^+ will move on the C^- surface, according to the polarization direction where C^+ and C^- corresponds to the ferroelectric domains that show upward and downward polarization, respectively. During positive poling, the applied field in pBTO points toward the substrate, aligning the ferroelectric domains with polarization downward from the surface (C^-), which in turn induces the formation of an internal depolarization field (E_{dep}) that opposes the polarization direction. To obtain charge compensation, E_{dep} promotes hole accumulation at the surface of pBTO, leading to upward band-bending. Therefore, positive poling enhances hole transfer from the ferroelectric surface to the electrolyte to participate in the water oxidation reaction, favoring the performance of pBTO as photoanodes as observed (Figure 6e).

However, the effect of positive poling is more evident in pBTO-5 compared to pBTO-0.2. Indeed, at 1.19 V *versus* RHE, +8 V EC poled pBTO-5 shows an increment of the photocurrent density of about 7 $\mu A/cm^2$ compared to the unpoled counterpart. On the other hand, the +8 V EC poling state of pBTO-0.2 shows a higher photocurrent density (8.6 $\mu A/cm^2$ at 1.19 V *vs* RHE) than the unpoled state (6.8 $\mu A/cm^2$ at 1.19 V *vs* RHE), but the increase of PEC response is not as significant as in pBTO-5. This suggests that the PEC performance cannot be changed drastically using EC poling from the as-produced state in the pBTO-0.2 sample (Figure 6f).

This evidence can be correlated to the PFM results previously reported for pBTO-5 and pBTO-0.2 thin films. In the pBTO-5 thin film, the almost complete domains switching observed is reflected in a greater enhancement in the PEC performance after positive poling, compared to pBTO-0.2, where the smaller pores and grains of pBTO-0.2 may make polarization switching more difficult.

https://doi.org/10.1021/acsami.1c17419
ACS Appl. Mater. Interfaces XXXX, XXX, XXX−XXX

After −8 V EC poling, pBTO-0.2 exhibits a reduced photocurrent density (4.5 μA/cm^2 at 1.19 V *vs* RHE) compared to the unpoled state (6.8 μA/cm^2 at 1.19 V *vs* RHE). Indeed, during negative poling, the applied electric field points to the pBTO surface, generating the formation of opposite E_{dep} which will create electron accumulation at the surface of pBTO and consequently downward band-bending. This leads to the presence of more electrons available for the water reduction reaction (Figure 6e) but suppresses hole injection and therefore photocurrent under anodic bias. This trend in terms of PEC response is also observed in pBTO-5 which shows slightly lower photocurrent density after −8 V EC poling (4 μA/cm^2 at 1.19 V *vs* RHE), compared to the unpoled state (4.4 μA/cm^2 at 1.19 V *vs* RHE) (Figure 6f).

CONCLUSIONS

In the present work, we synthesized and studied pBTO thin films prepared by a soft template-assisted sol−gel method, using different amounts of P123 organic sacrificial template. The concentration-dependent tuning of the porosity is evidenced by SEM analysis and spectroscopic ellipsometry, using air and water as surrounding mediums. The combination of these analyses indeed demonstrates the ability to tune the porosity of the resulting materials architectures in a range from 36% to 60%. XRD analysis and Raman spectroscopy are performed to confirm the tetragonal phase of the pBTO thin films, which is responsible for the ferroelectric behavior of BTO. In addition, using PFM, we verified the switching of spontaneous polarization in pBTO thin films, which appears more complete in pBTO-5 than pBTO-0.2. Owing to their controllable porosity, pBTO thin films are promising candidates as photoanodes, with all pBTO samples displaying enhanced photocurrent compared to a non-porous BTO film. We observed that when the quantity of the P123 block copolymer was increased, the PEC response gradually decreased, and this evidence can be related to the lower surface area in pBTO-5, compared to pBTO-0.2. Moreover, after performing +8 V EC poling, a clear improvement in the PEC performance of pBTO-5 compared to pBTO-0.2 was observed, which is in accordance with the PFM results obtained. This suggests that positive poling is very favorable when pBTO is used as a photoanode.

Thus, the controlled PEC response of a porous ferroelectric film *via* EC poling has been demonstrated, which opens up opportunities to tune and optimize the morphology of ferroelectric films for PEC applications while still maintaining the advantages conferred by ferroelectric polarization. For example, Rioult *et al.* have reported a PEC performance of *ca.* 50 μA/cm^2 at 1.2 V *versus* RHE for an epitaxial BTO thin film, prepared using atomic oxygen-assisted molecular beam epitaxy, which minimizes the defects in the films.[19] Therefore, the preparation of porous BTO thin films with tunable morphological properties, using methodologies that allow more precise control of the crystalline properties, could further maximize the obtained PEC performance. Moreover, pBTO thin films have a wide band gap and are therefore only UV-responsive, thus the tuning of the band gap *via* doping, or the use of the ever-increasing range of narrow band gap ferroelectrics currently under development[69−72] could be an excellent route to pursue in the future.

ASSOCIATED CONTENT

Supporting Information

The Supporting Information is available free of charge at https://pubs.acs.org/doi/10.1021/acsami.1c17419.

Additional experimental details and results of characterization using PFM, UV−vis spectroscopy, SE, SEM, and LSV measurements (PDF)

AUTHOR INFORMATION

Corresponding Author

Joe Briscoe − *School of Engineering and Material Science and Materials Research Institute, Queen Mary University of London, E1 4NS London, U.K.;* orcid.org/0000-0002-5925-860X; Email: j.briscoe@qmul.ac.uk

Authors

Adriana Augurio − *School of Engineering and Material Science and Materials Research Institute, Queen Mary University of London, E1 4NS London, U.K.*

Alberto Alvarez-Fernandez − *Department of Chemical Engineering, University College London, WC1E 7JE London, U.K.;* orcid.org/0000-0002-2607-3035

Vishal Panchal − *Bruker, CV4 9GH Coventry, U.K.*

Bede Pittenger − *AFM Unit, Bruker Nano Surfaces, 93117 Santa Barbara, California, United States*

Peter De Wolf − *AFM Unit, Bruker Nano Surfaces, 93117 Santa Barbara, California, United States*

Stefan Guldin − *Department of Chemical Engineering, University College London, WC1E 7JE London, U.K.;* orcid.org/0000-0002-4413-5527

Complete contact information is available at: https://pubs.acs.org/10.1021/acsami.1c17419

Notes

The authors declare no competing financial interest.

ACKNOWLEDGMENTS

This project received funding from the European Research Council (ERC) under the European Union's Horizon 2020 research and innovation programme (grant agreement no. 101001626). A.A.-F. and S.G. are grateful for funding by an EPSRC New Investigator Award (EP/R035105/1). The authors thank Dr. Richard Whiteley for carrying out XRD measurements.

REFERENCES

(1) Fujishima, A.; Honda, K. Electrochemical Photolysis of Water at a Semiconductor Electrode. *Nature* **1972**, *238*, 37−38.

(2) Grätzel, M. Photoelectrochemical Cells. *Nature* **2001**, *414*, 338−344.

(3) Morrison, S. R. *Electrochemistry at Semiconductor and Oxidized Metal Electrodes*, 1st ed.; Springer US: New York, 1980.

(4) Domen, K. Characterization of Photoexcitation Processes on Solid Surfaces. In *Surface Photochemistry*; Anpo, M., Ed.; John Wiley & Sons, 1996; pp 1−18.

(5) Schneider, J.; Matsuoka, M.; Takeuchi, M.; Zhang, J.; Horiuchi, Y.; Anpo, M.; Bahnemann, D. W. Understanding TiO_2 Photocatalysis Mechanisms and Materials. *Chem. Rev.* **2014**, *114*, 9919−9986.

(6) Sun, M.-H.; Huang, S.-Z.; Chen, L.-H.; Li, Y.; Yang, X.-Y.; Yuan, Z.-Y.; Su, B.-L. Applications of Hierarchically Structured Porous Materials from Energy Storage and Conversion, Catalysis, Photocatalysis, Adsorption, Separation, and Sensing to Biomedicine. *Chem. Soc. Rev.* **2016**, *45*, 3479−3563.

(7) Li, Y.; Fu, Z.-Y.; Su, B.-L. Hierarchically Structured Porous Materials for Energy Conversion and Storage. *Adv. Funct. Mater.* **2012**, *22*, 4634−4667.
(8) Zhang, Z.; Wang, C.-C.; Zakaria, R.; Ying, J. Y. Role of Particle Size in Nanocrystalline TiO_2-Based Photocatalysts. *J. Phys. Chem. B* **1998**, *102*, 10871−10878.
(9) Li, L.; Salvador, P. A.; Rohrer, G. S. Photocatalysts with Internal Electric Fields. *Nanoscale* **2014**, *6*, 24−42.
(10) Xu, T.; Niu, P.; Wang, S.; Li, L. High Visible Light Photocatalytic Activities Obtained by Integrating G-C_3N_4 with Ferroelectric $PbTiO_3$. *J. Mater. Sci. Technol.* **2021**, *74*, 128−135.
(11) Lines, M. E.; Glass, A. M. *Principles and Applications of Ferroelectrics and Related Materials*; Oxford University Press, 1997.
(12) Giocondi, J. L.; Rohrer, G. S. Spatial Separation of Photochemical Oxidation and Reduction Reactions on the Surface of Ferroelectric $BaTiO_3$. *J. Phys. Chem. B* **2001**, *105*, 8275−8277.
(13) Morris, M. R.; Pendlebury, S. R.; Hong, J.; Dunn, S.; Durrant, J. R. Effect of Internal Electric Fields on Charge Carrier Dynamics in a Ferroelectric Material for Solar Energy Conversion. *Adv. Mater.* **2016**, *28*, 7123−7128.
(14) Kalinin, S. V.; Bonnell, D. A.; Alvarez, T.; Lei, X.; Hu, Z.; Ferris, J. H.; Zhang, Q.; Dunn, S. Atomic Polarization and Local Reactivity on Ferroelectric Surfaces: A New Route toward Complex Nanostructures. *Nano Lett.* **2002**, *2*, 589−593.
(15) Inoue, Y.; Yoshioka, I.; Sato, K. Polarization Effects upon Adsorptive and Catalytic Properties. 1. CO Oxidation over Pd Deposited on $LiNbO_3$ Ferroelectrics. *J. Phys. Chem.* **1984**, *88*, 1148−1151.
(16) Burbure, N. V.; Salvador, P. A.; Rohrer, G. S. Photochemical Reactivity of Titania Films on $BaTiO_3$ Substrates: Origin of Spatial Selectivity. *Chem. Mater.* **2010**, *22*, 5823−5830.
(17) Burbure, N. V.; Salvador, P. A.; Rohrer, G. S. Photochemical Reactivity of Titania Films on $BaTiO_3$ Substrates: Influence of Titania Phase and Orientation. *Chem. Mater.* **2010**, *22*, 5831−5837.
(18) Cheng, X.; Dong, W.; Zheng, F.; Fang, L.; Shen, M. Enhanced Photocathodic Behaviors of $Pb(Zr_{0.20}Ti_{0.80})O_3$ Films on Si Substrates for Hydrogen Production. *Appl. Phys. Lett.* **2015**, *106*, 243901.
(19) Rioult, M.; Datta, S.; Stanescu, D.; Stanescu, S.; Belkhou, R.; Maccherozzi, F.; Magnan, H.; Barbier, A. Tailoring the Photocurrent in $BaTiO_3$/Nb:$SrTiO_3$ Photoanodes by Controlled Ferroelectric Polarization. *Appl. Phys. Lett.* **2015**, *107*, 103901.
(20) Cao, D.; Wang, Z.; Wen, L.; Mi, Y.; Lei, Y. Switchable Charge-Transfer in the Photoelectrochemical Energy- Conversion Process of Ferroelectric $BiFeO_3$ Photoelectrodes. *Angew. Chem., Int. Ed.* **2014**, *53*, 11027−11031.
(21) Suzuki, N.; Osada, M.; Billah, M.; Bando, Y.; Yamauchi, Y.; Hossain, S. A. Chemical Synthesis of Porous Barium Titanate Thin Film and Thermal Stabilization of Ferroelectric Phase by Porosity-Induced Strain. *J. Visualized Exp.* **2018**, 57441.
(22) Matavž, A.; Bradeško, A.; Rojac, T.; Malič, B.; Bobnar, V. Self-Assembled Porous Ferroelectric Thin Films with a Greatly Enhanced Piezoelectric Response. *Appl. Mater. Today* **2019**, *16*, 83−89.
(23) Castro, A.; Ferreira, P.; Rodriguez, B. J.; Vilarinho, P. M. The Role of Nanoporosity on the Local Piezo and Ferroelectric Properties of Lead Titanate Thin Films. *J. Mater. Chem. C* **2015**, *3*, 1035−1043.
(24) Ferreira, P.; Hou, R. Z.; Wu, A.; Willinger, M.-G.; Vilarinho, P. M.; Mosa, J.; Laberty-Robert, C.; Boissière, C.; Grosso, D.; Sanchez, C. Nanoporous Piezo- and Ferroelectric Thin Films. *Langmuir* **2012**, *28*, 2944−2949.
(25) Polking, M. J.; Han, M.-G.; Yourdkhani, A.; Petkov, V.; Kisielowski, C. F.; Volkov, V. V.; Zhu, Y.; Caruntu, G.; Paul Alivisatos, A.; Ramesh, R. Ferroelectric Order in Individual Nanometre-Scale Crystals. *Nat. Mater.* **2012**, *11*, 700−709.
(26) Singh, S.; Sangle, A. L.; Wu, T.; Khare, N.; MacManus-Driscoll, J. L. Growth of Doped $SrTiO_3$ Ferroelectric Nanoporous Thin Films and Tuning of Photoelectrochemical Properties with Switchable Ferroelectric Polarization. *ACS Appl. Mater. Interfaces* **2019**, *11*, 45683−45691.
(27) Singh, S.; Khare, N. Electrically Tuned Photoelectrochemical Properties of Ferroelectric Nanostructure $NaNbO_3$ Films. *Appl. Phys. Lett.* **2017**, *110*, 152902.
(28) Das, S.; Fourmont, P.; Benetti, D.; Cloutier, S. G.; Nechache, R.; Wang, Z. M.; Rosei, F. High Performance $BiFeO_3$ Ferroelectric Nanostructured Photocathodes. *J. Chem. Phys.* **2020**, *153*, 084705.
(29) Li, S.; Zhang, J.; Zhang, B.-P.; Huang, W.; Harnagea, C.; Nechache, R.; Zhu, L.; Zhang, S.; Lin, Y.-H.; Ni, L.; Sang, Y.-H.; Liu, H.; Rosei, F. Manipulation of Charge Transfer in Vertically Aligned Epitaxial Ferroelectric $KNbO_3$ Nanowire Array Photoelectrodes. *Nano Energy* **2017**, *35*, 92−100.
(30) Khan, M. A.; Kurchania, R.; Corkovic, S.; Zhang, Q.; Milne, S. J. Compaction of Lead Zirconate Titanate Sol-Gel Coatings. *Mater. Lett.* **2006**, *60*, 1463−1465.
(31) Zhang, Q.; Corkovic, S.; Shaw, C. P.; Huang, Z.; Whatmore, R. W. Effect of Porosity on the Ferroelectric Properties of Sol-Gel Prepared Lead Zirconate Titanate Thin Films. *Thin Solid Films* **2005**, *488*, 258−264.
(32) Suzuki, N.; Zakaria, M. B.; Torad, N. L.; Wu, K. C.-W.; Nemoto, Y.; Imura, M.; Osada, M.; Yamauchi, Y. Synthesis of Highly Strained Mesostructured $SrTiO_3$/$BaTiO_3$ Composite Films with Robust Ferroelectricity. *Chem.—Eur. J.* **2013**, *19*, 4446−4450.
(33) Songtanasit, R.; Taychatanapat, T.; Chatraphorn, S. Electrical Properties of Ultra-Thin TiO_2 Compact Layer on FTO for Perovskite Solar Cells. *J. Phys.: Conf. Ser.* **2017**, *901*, 012161.
(34) Tai, Q.; You, P.; Sang, H.; Liu, Z.; Hu, C.; Chan, H. L. W.; Yan, F. Efficient and Stable Perovskite Solar Cells Prepared in Ambient Air Irrespective of the Humidity. *Nat. Commun.* **2016**, *7*, 11105.
(35) Matějíček, J.; Kolman, B.; Dubský, J.; Neufuss, K.; Hopkins, N.; Zwick, J. Alternative Methods for Determination of Composition and Porosity in Abradable Materials. *Mater. Charact.* **2006**, *57*, 17−29.
(36) Raciti, R.; Bahariqushchi, R.; Summonte, C.; Aydinli, A.; Terrasi, A.; Mirabella, S. Optical Bandgap of Semiconductor Nanostructures : Methods for Experimental Data Analysis. *J. Appl. Phys.* **2017**, *121*, 234304.
(37) Khardani, M.; Bouaïcha, M.; Bessaïs, B. Bruggeman Effective Medium Approach for Modelling Optical Properties of Porous Silicon: Comparison with Experiment. *Phys. Status Solidi* **2007**, *4*, 1986−1990.
(38) Guldin, S.; Kolle, M.; Stefik, M.; Langford, R.; Eder, D.; Wiesner, U.; Steiner, U. Tunable Mesoporous Bragg Reflectors Based on Block-Copolymer Self-Assembly. *Adv. Mater.* **2011**, *23*, 3664−3668.
(39) Emmett, P. H.; Brunauer, S. The Use of Low Temperature van Der Waals Adsorption Isotherms in Determining the Surface Area of Iron Synthetic Ammonia Catalysts. *J. Am. Chem. Soc.* **1937**, *59* (8), 1553−1564.
(40) Datta, S.; Rioult, M.; Stanescu, D.; Magnan, H.; Barbier, A. Manipulating the Ferroelectric Polarization State of $BaTiO_3$ Thin Films. *Thin Solid Films* **2016**, *607*, 7−13.
(41) Alvarez-Fernandez, A.; Reid, B.; Suthar, J.; Choy, S. Y.; Jara Fornerod, M.; Mac Fhionnlaoich, N.; Yang, L.; Schmidt-Hansberg, B.; Guldin, S. Fractionation of Block Copolymers for Pore Size Control and Reduced Dispersity in Mesoporous Inorganic Thin Films. *Nanoscale* **2020**, *12*, 18455−18462.
(42) Reid, B.; Alvarez-Fernandez, A.; Schmidt-Hansberg, B.; Guldin, S. Tuning Pore Dimensions of Mesoporous Inorganic Films by Homopolymer Swelling. *Langmuir* **2019**, *35*, 14074−14082.
(43) Lokupitiya, H. N.; Jones, A.; Reid, B.; Guldin, S.; Stefik, M. Ordered Mesoporous to Macroporous Oxides with Tunable Isomorphic Architectures: Solution Criteria for Persistent Micelle Templates. *Chem. Mater.* **2016**, *28*, 1653−1667.
(44) Wemple, S. H. Polarization Fluctuations and the Optical-Absorption Edge in $BaTiO_3$. *Phys. Rev. B: Solid State* **1970**, *2*, 2679.
(45) Sharma, S.; Tomar, M.; Puri, N. K.; Gupta, V. Ultraviolet Radiation Detection by Barium Titanate Thin Films Grown by Sol-Gel Hydrothermal Method. *Sens. Actuators, A* **2015**, *230*, 175−181.

https://doi.org/10.1021/acsami.1c17419
ACS Appl. Mater. Interfaces XXXX, XXX, XXX−XXX

(46) Jiang, W.; Cai, W.; Lin, Z.; Fu, C. Effects of Nd-Doping on Optical and Photovoltaic Properties of Barium Titanate Thin Films Prepared by Sol-Gel Method. *Mater. Res. Bull.* **2013**, *48*, 3092−3097.
(47) Cai, W.; Fu, C.; Gao, J.; Guo, Q.; Deng, X.; Zhang, C. Preparation and Optical Properties of Barium Titanate Thin Films. *Phys. B* **2011**, *406*, 3583−3587.
(48) Sharma, H. B. Structural and Optical Properties of Sol-Gel Derived Barium Titanate Thin Film. *Int. J. Mod. Phys. B* **2007**, *21*, 1837−1849.
(49) Rahchamani, S. Z.; Dizaji, H. R.; Ehsani, M. H. Study of Structural and Optical Properties of ZnS Zigzag Nanostructured Thin Films. *Appl. Surf. Sci.* **2015**, *356*, 1096−1104.
(50) Akkari, F. C.; Brini, R.; Kanzari, M.; Rezig, B. High Absorbing $CuInS_2$ Thin Films Growing by Oblique Angle Incidence Deposition in Presence of Thermal Gradient. *J. Mater. Sci.* **2005**, *40*, 5751−5755.
(51) Zhong, Y.; Shin, Y. C.; Kim, C. M.; Lee, B. G.; Kim, E. H.; Park, Y. J.; Sobahan, K. M. A.; Hwangbo, C. K.; Lee, Y. P.; Kim, T. G. Optical and Electrical Properties of Indium Tin Oxide Thin Films with Tilted and Spiral Microstructures Prepared by Oblique Angle Deposition. *J. Mater. Res.* **2008**, *23*, 2500−2505.
(52) Wemple, S. H. Polarization Fluctuations and the Optical-Absorption Edge in $BaTiO_3$. *Phys. Rev. B: Solid State* **1970**, *2*, 2679−2689.
(53) Vaněček, M.; Poruba, A.; Remeš, Z.; Beck, N.; Nesládek, M. Optical Properties of Microcrystalline Materials. *J. Non-Cryst. Solids* **1998**, *227−230*, 967−972.
(54) Zdravkov, B.; Čermák, J.; Šefara, M.; Janků, J. Pore classification in the characterization of porous materials: A perspective. *Open Chemistry* **2007**, *5* (2), 385−395.
(55) Wemple, S. H.; Didomenico, M.; Camlibel, I. Dielectric and Optical Properties of Melt-Grown $BaTiO_3$. *J. Phys. Chem. Solids* **1968**, *29*, 1797−1803.
(56) Alvarez-Fernandez, A.; Reid, B.; Fornerod, M. J.; Taylor, A.; Divitini, G.; Guldin, S. Structural Characterization of Mesoporous Thin Film Architectures: A Tutorial Overview. *ACS Appl. Mater. Interfaces* **2020**, *12*, 5195−5208.
(57) Uchino, K.; Sadanaga, E.; Hirose, T. Dependence of the Crystal Structure on Particle Size in Barium Titanate. *J. Am. Ceram. Soc.* **1989**, *72*, 1555−1558.
(58) Begg, B. D.; Vance, E. R.; Nowotny, J. Effect of Particle Size on the Room-Temperature Crystal Structure of Barium Titanate. *J. Am. Ceram. Soc.* **1994**, *77*, 3186−3192.
(59) Suzuki, N.; Osada, M.; Billah, M.; Bando, Y.; Yamauchi, Y.; Hossain, S. A. Chemical Synthesis of Porous Barium Titanate Thin Film and Thermal Stabilization of Ferroelectric Phase by Porosity-Induced Strain. *J. Visualized Exp.* **2018**, No. e57441.
(60) Zhang, W. H.; Chen, L.; Tao, Y. T.; Zhang, W. H.; Chen, J.; Zhang, J. X. Raman Study of Barium Titanate with Oxygen Vacancies. *Phys. B* **2011**, *406*, 4630−4633.
(61) Suzuki, N.; Osada, M.; Billah, M.; Alothman, Z. A.; Bando, Y.; Yamauchi, Y.; Hossain, M. S. A. Origin of Thermally Stable Ferroelectricity in a Porous Barium Titanate Thin Film Synthesized through Block Copolymer Templating. *APL .Mater* **2017**, *5*, 076111.
(62) Solís, D.; Vigueras-Santiago, E.; Hernández-López, S.; Gómez-Cortés, A.; Aguilar-Franco, M.; Camacho-López, M. A. Textural , Structural and Electrical Properties of TiO_2 Nanoparticles Using Brij 35 and P123 as Surfactants. *Sci. Technol. Adv. Mater.* **2008**, *9*, 025003.
(63) Zeng, H. R.; Yu, H. F.; Tang, X. G.; Chu, R. Q.; Li, G. R.; Yin, Q. R. Piezoresponse Force Microscopy Studies of Nanoscale Domain Structures in Ferroelectric Thin Film. *Mater. Sci. Eng., B* **2005**, *120*, 104−108.
(64) Melo, M.; Araújo, E. B.; Shvartsman, V. V.; Shur, V. Y.; Kholkin, A. L. Thickness Effect on the Structure, Grain Size, and Local Piezoresponse of Self-Polarized Lead Lanthanum Zirconate Titanate Thin Films. *J. Appl. Phys.* **2016**, *120*, 054101.
(65) Neumayer, S. M.; Saremi, S.; Martin, L. W.; Collins, L.; Tselev, A.; Jesse, S.; Kalinin, S. V.; Balke, N. Piezoresponse Amplitude and Phase Quantified for Electromechanical Characterization. *J. Appl. Phys.* **2020**, *128*, 171105.
(66) Balke, N.; Maksymovych, P.; Jesse, S.; Kravchenko, I. I.; Li, Q.; Kalinin, S. V. Exploring Local Electrostatic Effects with Scanning Probe Microscopy: Implications for Piezoresponse Force Microscopy and Triboelectricity. *ACS Nano* **2014**, *8*, 10229−10236.
(67) Jesse, S.; Baddorf, A. P.; Kalinin, S. V. Switching Spectroscopy Piezoresponse Force Microscopy of Ferroelectric Materials. *Appl. Phys. Lett.* **2006**, *88*, 062908.
(68) Li, Y.; Li, J.; Yang, W.; Wang, X. Implementation of Ferroelectric Materials in Photocatalytic and Photoelectrochemical Water Splitting. *Nanoscale Horiz.* **2020**, *5*, 1174−1187.
(69) Rong, N.; Chu, M.; Tang, Y.; Zhang, C.; Cui, X.; He, H.; Zhang, Y.; Xiao, P. Improved Photoelectrocatalytic Properties of Ti-Doped $BiFeO_3$ Films for Water Oxidation. *J. Mater. Sci.* **2016**, *51*, 5712−5723.
(70) Huang, C.; Zhang, X.; Zhang, H.; Zhang, W.; Lan, C.; Li, M. Enhanced Photoelectrocatalytic Performance from Size Effects in Pure and La-Doped $BiFeO_3$ Nanoparticles. *Appl. Phys. A: Mater. Sci. Process.* **2020**, *126*, 273.
(71) Wani, W. A.; Kundu, S.; Ramaswamy, K.; Venkataraman, B. H. Optimizing Phase Formation of $BiFeO_3$ and Mn-Doped $BiFeO_3$ Nanoceramics via Thermal Treatment Using Citrate Precursor Method. *SN Appl. Sci.* **2020**, *2*, 1969.
(72) Huang, W.; Harnagea, C.; Tong, X.; Benetti, D.; Sun, S.; Chaker, M.; Rosei, F.; Nechache, R. Epitaxial Bi_2FeCrO_6 Multiferroic Thin-Film Photoanodes with Ultrathin p-Type NiO Layers for Improved Solar Water Oxidation. *ACS Appl. Mater. Interfaces* **2019**, *11*, 13185−13193.

https://doi.org/10.1021/acsami.1c17419
ACS Appl. Mater. Interfaces XXXX, XXX, XXX−XXX